NASA/TM—2005-213830

# Navier-Stokes Computations With One-Equation Turbulence Model for Flows Along Concave Wall Surfaces

Chi R. Wang
Glenn Research Center, Cleveland, Ohio

August 2005

## The NASA STI Program Office . . . in Profile

Since its founding, NASA has been dedicated to the advancement of aeronautics and space science. The NASA Scientific and Technical Information (STI) Program Office plays a key part in helping NASA maintain this important role.

The NASA STI Program Office is operated by Langley Research Center, the Lead Center for NASA's scientific and technical information. The NASA STI Program Office provides access to the NASA STI Database, the largest collection of aeronautical and space science STI in the world. The Program Office is also NASA's institutional mechanism for disseminating the results of its research and development activities. These results are published by NASA in the NASA STI Report Series, which includes the following report types:

- TECHNICAL PUBLICATION. Reports of completed research or a major significant phase of research that present the results of NASA programs and include extensive data or theoretical analysis. Includes compilations of significant scientific and technical data and information deemed to be of continuing reference value. NASA's counterpart of peer-reviewed formal professional papers but has less stringent limitations on manuscript length and extent of graphic presentations.

- TECHNICAL MEMORANDUM. Scientific and technical findings that are preliminary or of specialized interest, e.g., quick release reports, working papers, and bibliographies that contain minimal annotation. Does not contain extensive analysis.

- CONTRACTOR REPORT. Scientific and technical findings by NASA-sponsored contractors and grantees.

- CONFERENCE PUBLICATION. Collected papers from scientific and technical conferences, symposia, seminars, or other meetings sponsored or cosponsored by NASA.

- SPECIAL PUBLICATION. Scientific, technical, or historical information from NASA programs, projects, and missions, often concerned with subjects having substantial public interest.

- TECHNICAL TRANSLATION. English-language translations of foreign scientific and technical material pertinent to NASA's mission.

Specialized services that complement the STI Program Office's diverse offerings include creating custom thesauri, building customized databases, organizing and publishing research results . . . even providing videos.

For more information about the NASA STI Program Office, see the following:

- Access the NASA STI Program Home Page at ***http://www.sti.nasa.gov***

- E-mail your question via the Internet to help@sti.nasa.gov

- Fax your question to the NASA Access Help Desk at 301–621–0134

- Telephone the NASA Access Help Desk at 301–621–0390

- Write to:
  NASA Access Help Desk
  NASA Center for AeroSpace Information
  7121 Standard Drive
  Hanover, MD 21076

NASA/TM—2005-213830

# Navier-Stokes Computations With One-Equation Turbulence Model for Flows Along Concave Wall Surfaces

Chi R. Wang
Glenn Research Center, Cleveland, Ohio

National Aeronautics and
Space Administration

Glenn Research Center

August 2005

Available from

NASA Center for Aerospace Information
7121 Standard Drive
Hanover, MD 21076

National Technical Information Service
5285 Port Royal Road
Springfield, VA 22100

Available electronically at http://gltrs.grc.nasa.gov

# Navier-Stokes Computations With One-Equation Turbulence Model for Flows Along Concave Wall Surfaces

Chi R. Wang
National Aeronautics and Space Administration
Glenn Research Center
Cleveland, Ohio 44135

## Abstract

This report presents the use of a time-marching three-dimensional (3-D) compressible Navier-Stokes equation numerical solver with a one-equation turbulence model to simulate the flow fields developed along concave wall surfaces without and with a downstream extension flat wall surface. The 3-D Navier-Stokes numerical solver came from the NASA Glenn-HT code. The one-equation turbulence model was derived from the Spalart and Allmaras model. The computational approach was first calibrated with the computations of the velocity and Reynolds shear stress profiles of a steady flat plate boundary layer flow. The computational approach was then used to simulate developing boundary layer flows along concave wall surfaces without and with a downstream extension wall. The author investigated the computational results of surface friction factors, near surface velocity components, near wall temperatures, and a turbulent shear stress component in terms of turbulence modeling, computational mesh configurations, inlet turbulence level, and time iteration step. The computational results were compared with existing measurements of skin friction factors, velocity components, and shear stresses of the developing boundary layer flows. With a fine computational mesh and a one-equation model, the computational approach could predict accurately the skin friction factors, near surface velocity and temperature, and shear stress within the flows. The computed velocity components and shear stresses also showed the vortices effect on the velocity variations over a concave wall. The computed eddy viscosities at the near wall locations were also compared with the results from a two equation turbulence modeling technique. The inlet turbulence length scale was found to have little effect on the eddy viscosities at locations near the concave wall surface. The eddy viscosities, from the one-equation and two-equation modeling, were comparable at most stream-wise stations. The present one-equation turbulence model is an effective approach for turbulence modeling in the near solid wall surface region of flow over a concave wall.

## Introduction

The Gas Turbine Branch of NASA Glenn Research Center has developed the NASA Glenn-HT CFD Code for the prediction of gas turbine blade surface heat transfer. This Code used time-stepping Reynolds Averaged Navier-Stokes computational method (ref. 1) with a two-equation $k$-$\omega$ turbulence model (ref. 2) to simulate a turbine blade flow. Spalart and Allmaras (ref. 3) assembled an incompressible flow one-equation eddy viscosity model based on the turbulence modeling of two-dimensional (2-D) free shear layer, near wall finite/high Reynolds flows, and transition and tripping of laminar flow. With these assembling procedures, the present author believes that the one-equation eddy viscosity model has the potential for turbulence modeling of the Navier-Stokes numerical simulation of near surface flow along a turbine blade surface. Before the model could be used for turbulence modeling of a complex turbine blade flow, the turbulence model should be verified for its effectiveness to aid the Navier-Stokes computations of simple 3-D boundary layer flows. The turbulence intensity and length scale at the inlet of turbine blade and blade surface curvature play an important role in the flow development along the blade wall surface. The author has previously studied (refs. 4 to 6) the applications of the one–equation turbulence model and a 3-D Navier-Stokes numerical solver (ref. 1) for the simulations of boundary layer flow developments related to turbine blade flow field.

Based on the Spalart and Allmaras eddy viscosity model (ref. 3), this author derived a 3-D compressible one-equation eddy viscosity equation (ref. 4). The equation was written in a form similar to the compressible Navier-Stokes equation. The eddy viscosity equation was implemented into the computational procedures of a version of the NASA Glenn-HT code. Numerical computations were performed (ref. 4) to calculate the mean velocity of flat plate boundary layer flows with and without flow injection through discrete holes on the plate surface. The computational approach predicted the occurrence of a fully developed turbulent boundary layer velocity profile within the flow over a flat plate surface. The approach could also simulate successfully the effect of the injection fluid turbulence level on the mean velocity profile near an injection hole. Subsequently, this author used the computational approach to analyze the development of boundary layer flows along concave wall surfaces without (ref. 5) and with (ref. 6) a downstream recovery flat wall surface. With a global time step (ref. 1) used in these previous computational flow simulations, the computed friction factors, velocity, and the static temperatures at the near wall surface locations oscillated periodically in terms of the time iteration step and physical locations along the span-

wise direction. These results agreed well with similar results from existing experiments (refs. 7 to 9). The numerical approach was also found capable of capturing the vortices effect on the velocity variation and flow transition along a concave wall surface (ref. 7).

This paper describes the author's recent work to investigate further his previous observations of the results in references 4 to 6. The work explored the computational predictions, using the one-equation turbulence model (ref. 4), of the Reynolds shear stress component, the near wall surface temperature, and the occurrence of flow transition as the flow developed along a concave wall surface. The near wall eddy viscosities from the one-equation turbulence model were also compared with the results from a low Reynolds number two-equation turbulence modeling technique (ref. 10). First, the computed velocity and eddy viscosity profiles (ref. 4) were used to verify the ability to calculate the Reynolds shear stresses of a fully developed turbulent flat plate boundary layer flow. Then, a fine computational mesh was used to compute the skin friction factor, the Reynolds shear stress, the near wall surface temperature, and the mean flow velocity components within the developing flows over concave wall surfaces without and with a downstream extension wall surface. The computed skin friction factors, velocity components, near wall surface temperatures, and a component of Reynolds shear stress were compared with their existing results in the previous work (refs. 5 and 6) and in experiments (refs. 7 to 9). The comparisons showed that the accuracy of the numerical computations depended on the computational mesh configuration. With a fine mesh, the present computational approach could predict accurately the variations of velocity, Reynolds shear stress, near wall surface temperature, and the occurrence of flow transition. The present one-equation turbulence modeling did not consider the effect of the inlet turbulence length scale on the numerical computations. Alternately, the author used a low Reynolds number $k$-$\omega$ turbulence model (ref. 10) to compute the eddy viscosities within the flow over the concave wall surface. The author compared the eddy viscosities obtained from both the one-equation and two-equation turbulence modeling. The inlet turbulence length scale was found to have little effect on the turbulence modeling properties. The near wall surface eddy viscosities from the one-equation turbulence model were comparable to the eddy viscosities from the two equation turbulence modeling. Thus, the present one-equation turbulence model is an effective approach to model the turbulence eddy viscosities at near solid wall surface locations within a flow developed along a concave wall surface.

## Nomenclature

| | |
|---|---|
| $C_f$ | friction factor |
| $C_p$ | specific heat |
| $dV_s$ | shear layer velocity defect |
| $E_t$ | total energy |
| $h$ | turning duct height, 0.375 ft |
| $K$ | heat conductivity |
| $k$ | turbulence kinetic energy |
| $L$ | reference length, 0.833 ft or $h$ |
| $N$ | coordinate normal to wall surface |
| $m$ | flow rate |
| $n$ | number of time iteration steps |
| $p$ | pressure |
| Pr | Prandtl number |
| $Q_w$ | wall surface heat transfer rate |
| $R$ | universal gas constant |
| Re | Reynolds number/unit length, $\rho U_f/\mu$ |
| $\mathrm{Re}_L$ | Reynolds number based on $L$ |
| $\mathrm{Re}_x$ | Reynolds number based on $x$ |
| $S$ | Stream-wise coordinate, $s/h$ |
| $T$ | temperature |
| $U_f$ | free stream velocity |
| $u$, $v$, $w$ | velocity components in $x$, $y$, $z$ directions |
| $V_n$, $V_s$ | velocity components in $N$, $S$ directions |
| $\tilde{\nu}$ | working variable for eddy viscosity |
| $\nu_t$ | eddy viscosity, $\mu_t/\rho$ |
| $x$, $y$, $z$ | physical coordinates |
| $X$, $Y$, $Z$ | $x/L$, $y/L$, $z/L$ |
| $\chi$ | eddy viscosity parameter |
| $\Gamma$ | normalized time scale |
| $\mu$ | viscosity |
| $\delta$ | boundary layer thickness |
| $\rho$ | density |
| $\omega$ | turbulence dissipation rate |

**Subscripts**

| | |
|---|---|
| $f$ | freestream/inlet condition |
| $l$ | laminar flow |
| $o$ | stagnation condition |
| $r$ | reference condition |
| $t$ | turbulent flow |
| $w$ | wall surface condition |

## Computational Approach

The numerical computational procedures used in this work were similar to the procedures in the NASA Glenn-HT RANS Code. The Code solved the compressible 3-D Reynolds-Averaged Navier-Stokes equations using a four stage Runge-Kutta scheme in conjunction with accelerating techniques (ref. 1). The Code had the capabilities of multi-grid and multi-block to accelerate the steady flow computations. In addition, a very low level of artificial dissipation was guaranteed by eigenvalue scaling. The Code used the $k$ and $\omega$ equations (ref. 2) to model the eddy viscosity. Instead of the existing turbulence model in NASA-Glenn-HT code, a one-equation turbulence model was used here to calculate the eddy viscosities to model the turbulence

terms in the Navier-Stokes equations. The current numerical computational approach is described in the following sections.

**Navier-Stokes Equations**

The compressible Navier-Stokes Equations in Cartesian coordinates without body force or external heat addition were used to describe the flow fields. The equations were written as

$$\frac{\partial U}{\partial t}+\frac{\partial E}{\partial x}+\frac{\partial F}{\partial y}+\frac{\partial G}{\partial z}=0 \tag{1}$$

where

$$U=\begin{bmatrix}\rho\\ \rho u\\ \rho v\\ \rho w\\ E_t\end{bmatrix}$$

$$E=\begin{bmatrix}\rho u\\ \rho u^2+p-\tau_{xx}\\ \rho uv-\tau_{xy}\\ \rho uw-\tau_{xz}\\ (E_t+p)u-u\tau_{xx}-v\tau_{xy}-w\tau_{xz}-(k+k_t)\dfrac{\partial T}{\partial x}\end{bmatrix}$$

$$F=\begin{bmatrix}\rho v\\ \rho uv-\tau_{xy}\\ \rho v^2+p-\tau_{yy}\\ \rho vw-\tau_{yz}\\ (E_t+p)v-u\tau_{xy}-v\tau_{yy}-w\tau_{yz}-(k+k_t)\dfrac{\partial T}{\partial y}\end{bmatrix}$$

$$G=\begin{bmatrix}\rho w\\ \rho uw-\tau_{xz}\\ \rho vw-\tau_{yz}\\ \rho w^2+p-\tau_{zz}\\ (E_t+p)w-u\tau_{xz}-v\tau_{yz}-w\tau_{zz}-(k+k_t)\dfrac{\partial T}{\partial z}\end{bmatrix}$$

The components of the shear stress were given by

$$t_{xx}=\frac{2}{3}(\mu_l+\mu_t)\left(2\frac{\partial u}{\partial x}-\frac{\partial v}{\partial y}-\frac{\partial w}{\partial z}\right)$$

$$\tau_{yy}=\frac{2}{3}(\mu_l+\mu_t)\left(2\frac{\partial v}{\partial y}-\frac{\partial u}{\partial x}-\frac{\partial w}{\partial z}\right)$$

$$\tau_{zz}=\frac{2}{3}(\mu_l+\mu_t)\left(2\frac{\partial w}{\partial z}-\frac{\partial u}{\partial x}-\frac{\partial v}{\partial y}\right)$$

$$\tau_{xy}=(\mu_l+\mu_t)\left(\frac{\partial u}{\partial y}+\frac{\partial v}{\partial x}\right)=\tau_{yx}$$

$$\tau_{yz}=(\mu_l+\mu_t)\left(\frac{\partial v}{\partial z}+\frac{\partial w}{\partial y}\right)=\tau_{zy}$$

$$\tau_{xz}=(\mu_l+\mu_t)\left(\frac{\partial w}{\partial x}+\frac{\partial u}{\partial z}\right)=\tau_{zx}$$

The Reynolds analogy

$$k+k_t=C_p\left(\frac{\mu_l}{\mathrm{Pr}_l}+\frac{\mu_t}{\mathrm{Pr}_t}\right)$$

was used to relate the thermal conductivity and viscosity. $\mathrm{Pr}_l$ and $\mathrm{Pr}_t$ were the laminar and the turbulent Prandtl numbers.

The Navier-Stokes equations and their constituent equations were rewritten in a curvilinear coordinate system (ref. 1). These equations were then used in a finite-volume formulation (ref. 1) for numerical computations.

**One-Equation Turbulence Model**

Assuming the original version (ref. 3) of the eddy viscosity transport equation was applicable for compressible flow, the author wrote the transport equation, in terms of a working variable $\tilde{\nu}$, as

$$\begin{aligned}&\frac{\partial}{\partial t}(\rho\tilde{\nu})+\frac{\partial}{\partial x}(\rho u\tilde{\nu})+\frac{\partial}{\partial y}(\rho v\tilde{\nu})+\frac{\partial}{\partial z}(\rho w\tilde{\nu})\\ &=\frac{\partial}{\partial x}\left[\frac{\rho(\nu+\tilde{\nu})}{\sigma}\frac{\partial\tilde{\nu}}{\partial x}\right]+\frac{\partial}{\partial y}\left[\frac{\rho(\nu+\tilde{\nu})}{\sigma}\frac{\partial\tilde{\nu}}{\partial y}\right]\\ &+\frac{\partial}{\partial z}\left[\frac{\rho(\nu+\tilde{\nu})}{\sigma}\frac{\partial\tilde{\nu}}{\partial z}\right]+\rho C_{b1}(1-f_{t2})\tilde{S}\tilde{\nu}\\ &-\rho\left(C_{w1}f_w-C_{b1}f_{t2}/\kappa^2\right)(\tilde{\nu}/d)^2+\rho f_{t1}\Delta u^2\end{aligned} \tag{2a}$$

The above equation omitted the contribution (ref. 3) of $(\mathrm{grad}\,\tilde{\nu})^2$ to the turbulence modeling and substituted with $\tilde{\nu}$ for the diffusion coefficient (ref. 3). The eddy viscosity, $\nu_t=\mu_t/\rho$, was related to the working variable, $\tilde{\nu}$, through the equation

$$\nu_t=\tilde{\nu}f_{v1}$$

where $f_{v1} = \chi^3/\left(\chi^3 + {C_{v1}}^3\right)$, $\chi = \tilde{\nu}/\nu$ and $\nu$ is laminar kinematic viscosity.

The production term, $\tilde{S}$, is given by

$$\tilde{S} = S + \left(\tilde{\nu}/\kappa^2 d^2\right) f_{v2}$$

$S$ is the magnitude of the vorticity, $d$ is the distance to the wall, and

$$f_{v2} = 1 - \chi/\left(1 + \chi f_{v1}\right)$$

The destruction function, $f_w$, is given by

$$f_w = g\left(\frac{1 + {C_{w3}}^6}{g^6 + {C_{w3}}^6}\right)^{1/6}$$

where $g = r + C_{w2}\left(r^6 - r\right)$ and $r = \tilde{\nu}/\left(\tilde{S}\kappa^2 d^2\right)$.

The transition functions are

$$f_{t1} = C_{t1} g_t \exp\left(-C_{t2}\left({\omega_t}^2/\Delta u^2\right)\left(d^2 + {g_t}^2 d^2\right)\right)$$
$$f_{t2} = C_{t3}\exp\left(-C_{t4}\chi^2\right)$$

where $g_t = \min\left(0.1, \Delta u/\omega_t \Delta x\right)$.

In the transition functions, $\omega_t$ is the vorticity at the surface and $\Delta x$ is the grid spacing along the $x$ direction. The velocity difference between a field point and the surface was $\Delta u$.

Spalart and Allmaras (ref. 3) used the following set of empirical constants:

$$C_{b1} = 0.1355, C_{b2} = 0.622, \sigma = 2/3, \kappa = 0.41$$
$$C_{w1} = C_{b1}/\kappa^2 + \left(1 + C_{b2}\right)/\sigma, C_{w2} = 0.3, C_{w3} = 2,$$
$$C_{v1} = 7.1, C_{t1} = 1, C_{t2} = 2, C_{t3} = 1.1, C_{t4} = 2.$$

The turbulence transport equation, equation (2a) has the form similar to the compressible flow Navier-Stokes equations. The present author implemented equation (2a) in the Glenn-HT code to model the turbulence terms in the 3-D compressible Navier-Stokes equations. Similar to the manipulations of the Navier-Stoke equations in the Glenn HT-Code, equation (2a) was first non-dimensionalized with reference properties at the stagnation conditions:

$$T_r = T_0, p_r = p_0, u_r = \sqrt{RT_0}\ , \nu_r = \nu$$

and a length scale $L$. Equation (2a) becomes

$$\begin{aligned}
&\frac{\partial}{\partial \Gamma}\left(\hat{\rho}\hat{\tilde{\nu}}\right) + \frac{\partial}{\partial X}\left[\hat{\rho}\hat{U}\hat{\tilde{\nu}} - \frac{\hat{\rho}}{\mathrm{Re}_L}\left(\hat{\nu} + \hat{\tilde{\nu}}\right)\frac{\partial \hat{\tilde{\nu}}}{\partial X}\right] \\
&\quad + \frac{\partial}{\partial Y}\left[\hat{\rho}\hat{V}\hat{\tilde{\nu}} - \frac{\hat{\rho}}{\mathrm{Re}_L}\left(\hat{\nu} + \hat{\tilde{\nu}}\right)\frac{\partial \hat{\tilde{\nu}}}{\partial Y}\right] \\
&\quad + \frac{\partial}{\partial Z}\left[\hat{\rho}\hat{W}\hat{\tilde{\nu}} - \frac{\hat{\rho}}{\mathrm{Re}_L}\left(\hat{\nu} + \hat{\tilde{\nu}}\right)\frac{\partial \hat{\tilde{\nu}}}{\partial Z}\right] \\
&\quad = C_{b1}\left(1 - f_{t2}\right)\hat{\rho}\hat{\tilde{\nu}}\bar{S}^{0.5} \\
&\quad + \frac{C_{b1}}{\mathrm{Re}_L}\frac{\hat{\rho}\hat{\tilde{\nu}}^2}{\hat{d}^2\kappa^2}\left(1 - f_{t2}\right)\left[1 - \chi/\left(1 + \chi f_{v1}\right)\right] \\
&\quad - \frac{1}{\mathrm{Re}_L}\frac{\hat{\rho}\hat{\tilde{\nu}}^2}{\hat{d}^2}\left(C_{w1} f_w - \frac{C_{b1}}{\kappa^2} f_{t2}\right) \\
&\quad + \mathrm{Re}_L\,\hat{\rho} f_{t1}\Delta\hat{U}^2 L
\end{aligned} \tag{2b}$$

where $\hat{\rho}, \hat{\nu}, \hat{d}$, and $\hat{\tilde{\nu}}$ are dimensionless quantities (with respect to the reference conditions and $L$) and

$$\bar{S} = \left(\frac{\partial \hat{W}}{\partial Y} - \frac{\partial \hat{V}}{\partial Z}\right)^2 + \left(\frac{\partial \hat{U}}{\partial Z} - \frac{\partial \hat{W}}{\partial X}\right)^2 + \left(\frac{\partial \hat{V}}{\partial X} - \frac{\partial \hat{U}}{\partial Y}\right)^2$$

Equation (2b) showed that $\mathrm{Re}_L$ influenced the turbulence modeling. This was consistent with the dependence of $C_{b1}$, $C_{b2}$, and $C_{t1}$ on the Reynolds number (ref. 3). The present author further assumed that the empirical constants, $C_{t2}, C_{t3}, C_{t4}, C_{w2}, C_{v1}, \kappa$, and $\sigma$ in equation (2b) had the same values as they were in reference 3. The values for the empirical constants, $C_{b1}$, $C_{b2}$, and $C_{t1}$ were calibrated (ref. 4) for turbulent flat plate boundary layer flow. Computations, with $C_{b1}$ = 0.1 or 0.16, $C_{b2}$ = 0 or 0.622 and $C_{t1}$ = 0.1 did not predict a significant change in the $U$ values. However, the computations, with $C_{t1}=10^{-5}$, predicted a reduction of the mean velocity at the near surface locations and predicted better the skin friction factors ($C_f = 3\times10^{-3}$) at downstream stations. Although $C_{t1}$ had a small value, $\mathrm{Re}_L \times C_{t1}$ could have a large value and it was consistent with the assembling of the turbulence transport equation (ref. 3).

The eddy-viscosity equation was also used in the computations of the flows developed along concave wall surface without and with downstream flat plate wall surface. However, the following set of empirical constants,

$$C_{b1} = 0.160,\ C_{b2} = 0.622,\ \sigma = 2/3,\ \kappa = 0.41,$$
$$C_{w1} = C_{b1}/\kappa + (1 + C_{b2})/\sigma,\ C_{w2} = 0.3,\ C_{w3} = 2.,$$
$$C_{v1} = 7.1,\ C_{t1} = 0.00001,\ C_{t2} = 2.,\ C_{t3} = 1.1,\ C_{t4} = 2,$$

was assumed in the computations. For the computations of the boundary layer flows along the concave wall surfaces, $C_{t3}$ = 0 was assumed for turbulence modeling (ref. 3).

The eddy viscosity modeling equation (2b) was rewritten in the curvilinear coordinate system as it was applied to the Navier-Stokes equations. The Navier-Stokes solver of the NASA Glenn-HT Code was updated to solve simultaneously the Navier-Stokes Equations and the eddy viscosity transport equation.

### Numerical Schemes

Accurate and efficient numerical computational schemes to solve the Navier-Stokes equations were developed (ref. 1) for the NASA Glenn-HT code. The present author only used some of the numerical schemes in this work. The schemes used here are briefly described in below.

A finite volume approach was used to discretize the governing equations. Fourth order cell center spatial discretization scheme was used in the present computations. The domain was divided into hexahedrons (cells). Flow variables were stored at the cell centers. On each cell face the convective and diffusive fluxes were calculated after computing the necessary quantities at the face center. Those quantities were obtained by averaging of adjacent cell-center values of the dependent variables. The system of discretized equations was advanced in time using an explicit four stage Runge-Kutta scheme (ref. 1) to reach steady state solutions of the flow variables. The local time step limit, $\Delta t$, was computed with both the convective, $\Delta t_c$ and diffusive, $\Delta t_d$ contributions as $\Delta t = C_0 \ (\Delta t_c \ \Delta t_d/(\Delta t_c + \Delta t_d))$. The mathematical expressions for the convective and diffusive contributions could be found in reference 1. $C_0$ was a constant and was taken to be Courant-Friedrich-Levy (CFL) number. CFL = 1 was used in all the computations here. The maximum of the local time steps within the domain was used in the time-marching scheme to facilitate the steady state calculations. Artificial dissipation and residual smoothing (ref. 1) were also employed in the computations. The present author used one block and single grid in the computations. The multi-grid and multi-block options were not considered in this work. The present author used 2 different computational mesh configurations respectively in each flow computation and investigated the effect of the computational mesh configuration on the computations.

### Boundary Conditions

Although three different flow fields were considered in this work, all the computational domains consisted of inlet and exit planes, wall surfaces and symmetric planes. Since a fourth order cell-center scheme was used for spatial discretization in the numerical schemes. The numerical computations required flow properties at two phantom cell centers immediately outside of the domain surfaces. These properties were specified with the following approaches.

It was assumed that the cross flow velocity components were zero at the inlet phantom cell centers. Their static pressures and mass flow rates were set to the first interior cell centers' static pressures and mass flow rates computed from previous time iteration. The density and total energy were then computed from the pressure and velocity with isentropic flow relationships. A uniform turbulent eddy viscosity parameter $\chi_i$, of the order of 0.1 was imposed at the inlet phantom cell enters.

For the computations of the flows over the concave wall surfaces, flow symmetry was assumed at the far field domain surface. The flow properties at the phantom cell center next to the plane of symmetry were simply set to their properties at the interior cell centers adjacent to the boundary surface.

A zero normal pressure gradient was assumed at the wall surface and the linearization approach (ref. 11) was used to set the velocity and the density at the phantom cell centers. The constant wall temperature condition was used in computations and the wall surface temperature was 4 percent larger than the room temperature.

Flow symmetry was assumed at the domain surface along the $Z$ direction and at the far field domain surface along the $N$ direction. The flow properties at the Phantom cell centers next to these domain surfaces were set to their values at the interior cell centers adjacent to the boundary surfaces.

A uniform static pressure was imposed at the exit plane. The other mean flow properties at the down stream phantom cell centers were extrapolated (ref. 11) from interior values and the exit static pressure. The exit pressure level for each flow field considered here is given in the following Results and Discussion section. It was further assumed that the turbulent eddy viscosity values at the downstream phantom cell centers were the same as the eddy viscosity value at the first interior cell next to the exit plane.

## Results and Discussions

The numerical computations provided mean velocity components, mean temperatures, and eddy viscosities within 3 different flows. The velocity, temperature, and eddy viscosity were studied for the predictions of the existing measurements of near wall surface velocity, the Reynolds shear stress, friction factor, and wall surface heat transfer rate. The following sections describe the computational predictions and their comparisons with measurements.

### Flat Plate Turbulent Boundary Layer Flow

The computational procedures were used previously (ref. 4) to investigate the occurrence of a fully developed turbulent boundary layer velocity profile within a flow over a flat plate surface. The computations predicted approximately the law of the wall or the $1/7^{th}$ velocity profile at a distance of $21L$ ($L$ = 0.833 ft) from the plate leading edge. The computed velocity and eddy viscosity profiles at this stream-wise station were used here to study the calculation of the Reynolds shear stress profile within a fully developed turbulent boundary layer.

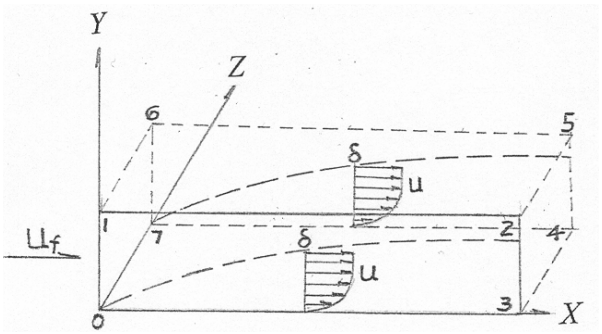

Figure 1.—Schematic of domain, 0-1-2-3-4-5-6-7.

Some of the important parameters of the previous computations were summarized here. The computations were performed with one physical domain, figure 1. The domain had a physical dimension of 42, 0.7, and 0.7 along the *X*, *Y*, and *Z* directions.

TABLE I.—MESH CONFIGURATIONS FOR FLAT PLATE BOUNDARY LAYER FLOW COMPUTATIONS.

| Mesh ID | Domain Size | Node Size | Node Packing at |
|---|---|---|---|
| 1 | 42, 0.7, 0.7 | 120, 100, 6 | $Y = 0, 0.7$ |
| 2 | 42, 0.7, 0.7 | 120, 100, 6 | $0 < Y < 0.05$ |

Two different computational meshes, table I, were used respectively to perform the computations. The meshes had the same node dimensions (120 in *X* direction, 100 in *Y* direction, and 6 in *Z* direction). The nodes were equally distributed along the *X* and *Z* directions but the meshes had different node distributions along the *Y*-direction. In mesh 1, the nodes along the *Y* direction were packed at the near wall ($Y = 0$) and free-stream locations ($Y = 0.7$). In Mesh 2, the nodes were packed only at near wall ($0 < Y < 0.05$) locations. The free stream Reynolds number was $3\times10^5$/ft to ensure the occurrence of a turbulent boundary layer flow. With either mesh configuration, the computations predicted a skin friction factor, $C_f \approx 3\times10^{-3}$ at $X = 21$. The free-stream Reynolds number at $X = 21$ was $5.2\times10^6$. This $C_f$ value agreed with the friction factor of a fully developed turbulent boundary layer flow. The profiles of mean velocity and eddy viscosity variations along the *Y* direction at $X = 21$ were shown in figures 2a and b. The velocity profile indicated a boundary layer thickness, δ of 0.35 *L* at this stream-wise station. This boundary layer thickness was the same as it was evaluated with the correlation of the boundary layer thickness and Reynolds number (ref. 12). The computed velocity profiles were also compared with the Law of the Wall and the 1/7th Law in figure 2b.

In the present work, the author used the mean velocity and eddy viscosity profiles in figures 2a and b to calculate the Reynolds shear stress component, $-\overline{u'v'}$ at locations across the boundary layer thickness. The Reynolds shear stress was computed from

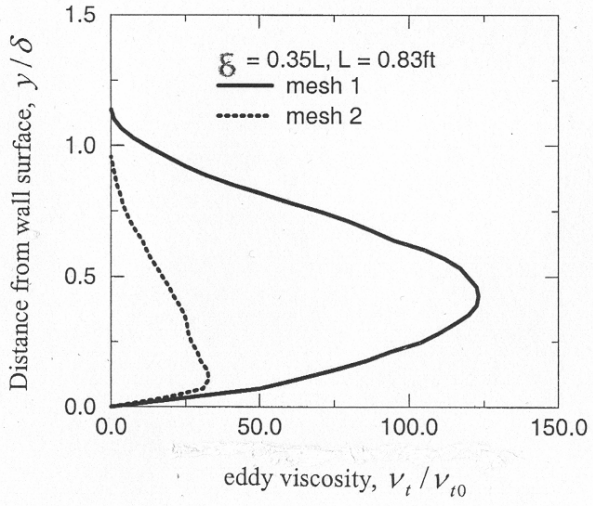

Figure 2a.—Boundary layer eddy viscosity profiles at $x/L = 21$.

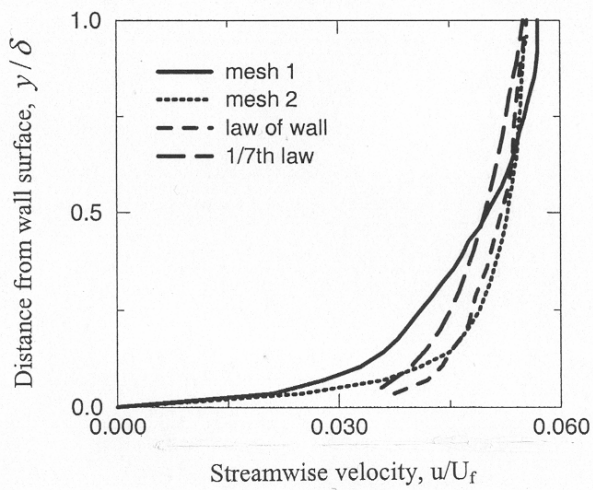

Figure 2b.—Boundary layer velocity profiles at $x/L = 21$.

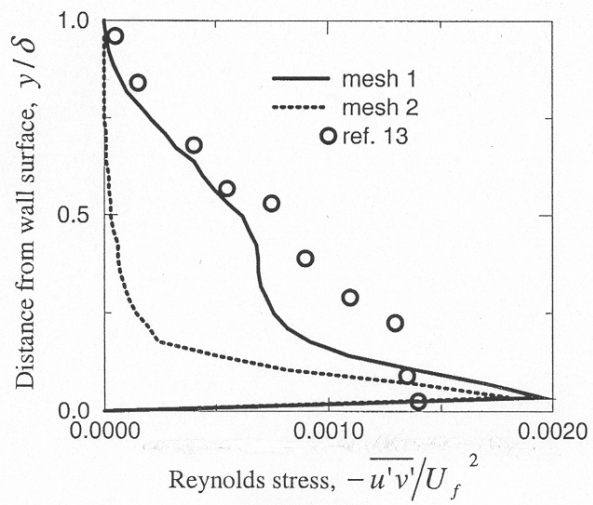

Figure 2c.—Boundary layer Reynolds shear stress profiles at $x/L = 21$.

$$-\overline{u'v'} = \nu_t\left(\partial u/\partial y + \partial v/\partial x\right) \quad (3)$$

Figure 2c shows the computed Reynolds shear stress profiles in terms of the dimensionless parameter, $-\overline{u'v'}/U_f{}^2$, $y/\delta$ and mesh configurations. Experimental results (ref. 13) of the Reynolds shear stress within a turbulent boundary layer flow, with $Re_x = 4.2\times10^6$, were also shown in figure 2c.

The results in figures 2a, b, and c show that computations, with two different meshes, predicted the same $u$, $\nu_t$, and $-\overline{u'v'}/U_f{}^2$ at near wall surface locations ($y/\delta < 0.05$). The computations, using mesh 1 predicted rapid growth in eddy viscosities (fig. 2a) at $0.05 < y/\delta < 0.5$ locations. The large eddy viscosity was associated with low mean velocities (fig. 2b). The velocity profile was close to the $1/7^{th}$ law of the wall profile. Large Reynolds shear stresses (fig. 2c) were calculated according to the velocity and eddy viscosity profiles. The computed Reynolds shear stresses agreed well with their measurements (ref. 13). The computations, using mesh 2, predicted a low eddy viscosity (fig. 2a) and a high velocity (fig. 2b) within the boundary layer. The velocity profile at $y/\delta > 0.1$ agreed well with the law of the wall profile (fig. 2b). The computed Reynolds shear stresses (fig. 2c) at $y/\delta > 0.05$ locations decreased rapidly along the $y$ direction and the shear stresses were smaller than the measurements. The results in figures 2a, b, and c showed that mesh configuration could affect the eddy viscosity, velocity, and Reynolds shear stress computations.

**Flow Over Concave Wall**

The author previously (refs. 5 and 6) used the computational methods to simulate existing experiments of free-stream turbulence and concave curvature effects on heated and transitional boundary layers (refs. 7 and 8). A sketch of the experimental flow filed and computational domain was shown in figure 3. The height, h, was 0.375 ft. The previous computational work showed the effect of computational mesh on the computational approach to predict the mean flow properties. The present work used a fine computational mesh to further explore the accurate predictions of near wall surface mean velocity, near surface temperature, and the Reynolds stress.

In the present work, the computations were performed with a fine mesh which has 205 nodes in $S$ direction, 101 nodes in $N$ direction and 57 nodes in $Z$ direction. Along $N$ direction, 33 nodes were packed in $0 < N < 0.01$, the first node from the wall surface was at $N = 0.0001$ location and the node spacing was 0.0175 at $N = 0.5$. The inlet turbulence parameter, $\chi_i$ and the downstream static pressure, $p_d$ were 0.075 and 0.96 respectively and these values were the same as they were in the previous work (ref. 6). Some of the present computational results were than compared with similar results from the previous work (ref. 6) with a different computational mesh configuration (mesh 4). Table II compares some of the important parameters between the two computational mesh configurations.

TABLE II.—MESH CONFIGURATIONS FOR FLOW OVER CONCAVE WALL SURFACE.

| Mesh ID | Packing $S = 0$ | Packing $S = 12.5$ | Packing $N = 0$ | Packing $N = 0.5$ |
|---|---|---|---|---|
| 3 | 0.059 | 0.089 | 0.0001 | 0.0175 |
| 4 | 0.059 | 0.089 | 0.0001 | 0.0300 |
| 3 | Nodes | 205 in $S$ | 101 in $N$ | 57 in $Z$ |
| 4 | Nodes | 205 in $S$ | 61 in $N$ | 57 in $Z$ |

With mesh 3, the computed values of skin friction factors converged when the computations proceeded to about 20,000 steps of time iteration. As an example, the $C_f$ values at 3 different iteration steps, $n$ = 19,800, 20,000, and 20,200 and at locations along the $S$ direction at $Z = 0.044$ are shown in figure 4a. The $C_f$ values at four $S$ stations from existing experiments (ref. 7) are also plotted in figure 4a to verify the accuracy of the computed $C_f$ values. The computed $C_f$ values jumped to large values at $S = 3$ station. Experiments (ref. 7) showed that flow transition occurred at this stream-wise station. Thus, the present computations with mesh 3 predicted the transition occurrence and reduced $C_f$ values to their experimental values at greater downstream stations ($S > 4$).

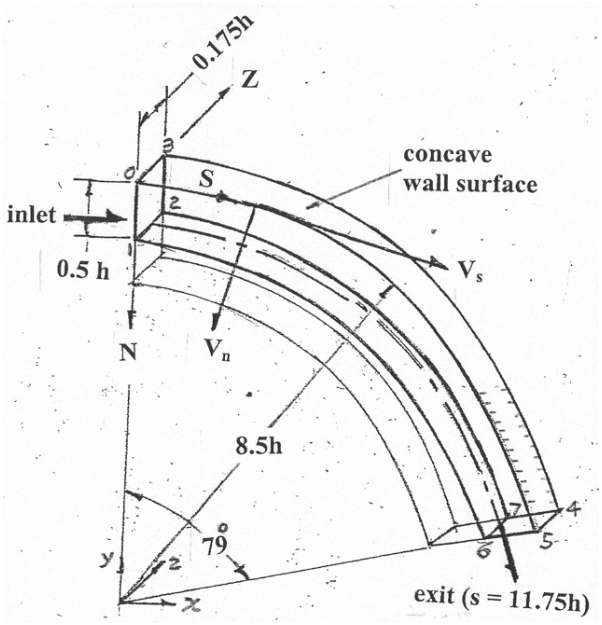


Figure 3.—Schematic of flow over concave wall and computational domain, 0-3-4-5-6-7-2-1.

To investigate the mesh effect on the computations, the computed $C_f$ values from the previous computations (ref. 6) with mesh 4 are shown in figure 4b. Mesh 4 had 205 nodes in $S$ direction and 57 nodes in $Z$ direction. There were only 61 nodes in $N$ direction and 23 nodes were packed in $0 > N > 0.01$ region. The second node was 0.0001 from the wall surface. The node spacing was stretched to 0.03 at far field boundary ($N$ = 0.5). Figure 4b showed that the computed $C_f$ values at $2 < S < 10$ stations oscillated at $n$ = 13,700, 14,200, and 14,650 steps of time iteration. Mesh 4 had less nodes along the $N$ direction and the computations did not predict a jump in the $C_f$ value at $S$ = 3 station. Thus, the computational approach required a relatively large numbers of nodes along the $N$ direction to predict accurately the flow transition location and stable friction factors at locations along the stream-wise direction.

The computed $C_f$ values (with mesh 3) at locations along $S$ direction at $n$ = 20,000 and at 3 span-wise $Z$ stations ($Z$ = 0.06, 0.044, and 0.088) are shown in figure 5. The $C_f$ values peaked at $S$ = 3 and 4 stations. The $C_f$ values varied periodically along the $Z$ direction at most $S$ stations. Since $C_f$ was computed from $V_s$, the results in figure 5 indicated that $V_s$ at the near wall surface locations could vary periodically along $Z$ direction.

Figures 6a and b show the $V_s$ variations at $N$ = 0.0025 and $0 < Z < 0.1$ locations at $S$ = 3.12 and $S$ = 5.35. The computed $V_s$ values with mesh 3 and at $n$ = 20,000, are presented in figure 6a and the computed $V_s$, with mesh 4 and at $n$ = 14,650, are presented in figure 6b. These results were also compared with the measurements of the velocity components (ref. 7). Figure 6a shows that, at $S$ = 3.12, the computed $V_s$ agrees well with the $V_s$ measurements and at $S$ = 5.35, the computed $V_s$ varied periodically at the span-wise locations. The measurements did not clearly shows the span-wise periodic $V_s$ variation at $S$ = 5.35 station. Figure 6a also shows good agreement among the computed and experimental $V_s$ values at $Z$ = 0.044. This was consistent with the results of friction factor presented in figure 4a. Comparisons between the results in figures 6a and b shows that computational mesh configuration affected the accuracy of the $V_s$ computations. Computations with 205, 101, and 57 mesh dimensions needed 20,000 time iteration steps to reach a converged solution. This simulated more closely the near wall $V_s$ span-wise variations at $S$ = 3.12 and 5.35 stations.

The computations used a constant temperature, $T_w/T_r$ = 1.04, as the temperature boundary condition at the wall surface. This wall temperature boundary condition was the same as the wall temperature of the experiment (ref. 7). The experiments applied a constant heat flux, $Q_w$ = 150 W/m$^2$ to maintain the wall surface temperature condition.

Assuming the one–dimensional heat conduction relation was valid between the wall surface and the first computational cell center locations, the surface heat transfer rate is given with

$$Q_w = -K\left(\partial T / \partial N\right)_{N=0} \qquad (4)$$

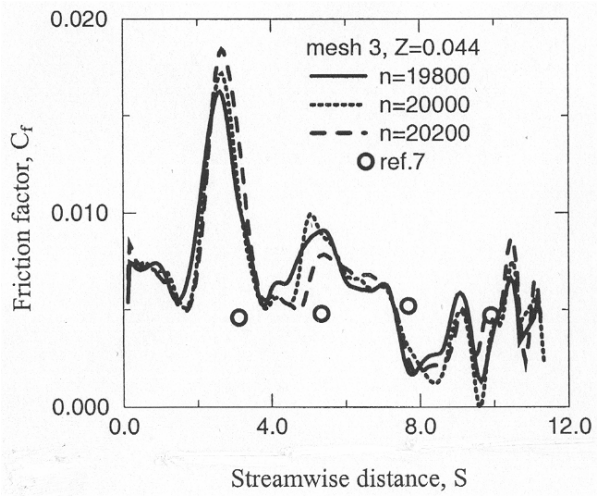


Figure 4a.—Friction factors computed with mesh 3.

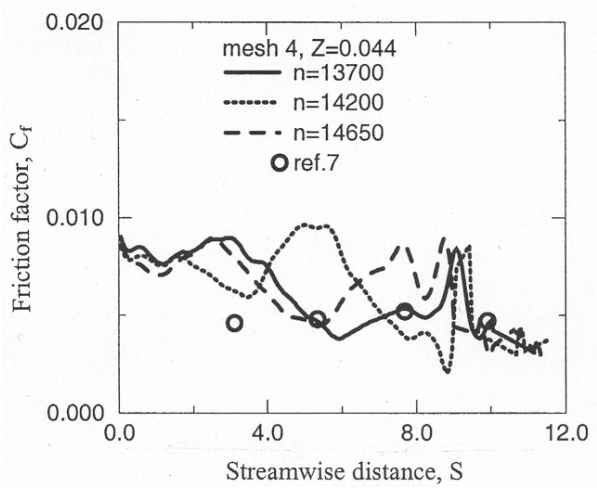


Figure 4b.—Friction factors computed with mesh 4.

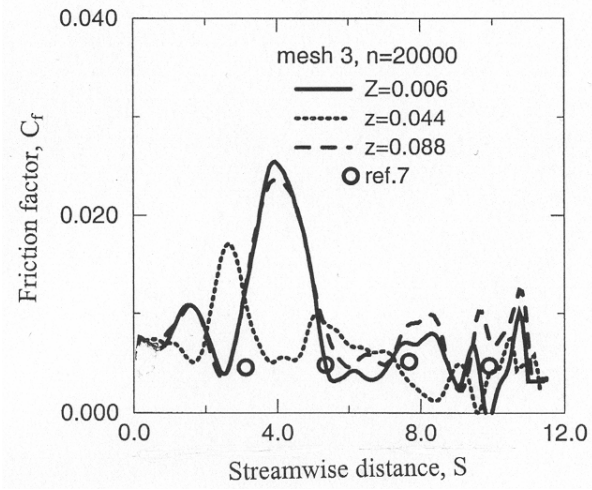


Figure 5.—Friction factors at stream-wise stations, mesh 3.

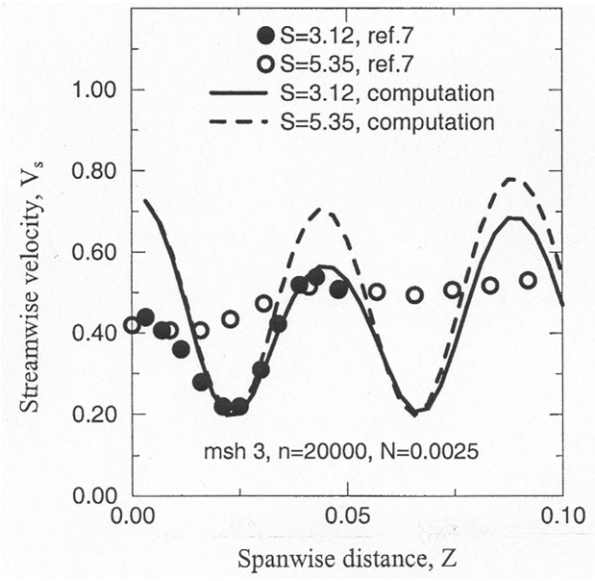


Figure 6a.—Spanwise $V_s$ variations at $N$ =0.0025, $S$ = 3.12, 5.35, $n$ = 20,000 and mesh 3.

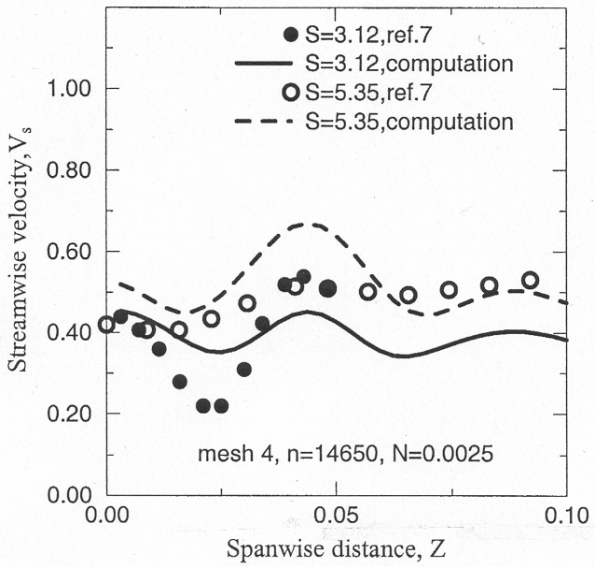


Figure 6b.—Spanwise $V_s$ variations at $N$ =0.0025, $S$ = 3.12, 5.35, $n$ = 14,650 and mesh 4.

Assuming that the temperature varied linearly at locations between the wall surface and the first cell center locations, equation (4) and the experimental $Q_w$ value were used to calculate the first cell center (at $N$ = 0.00005) temperature. The resulting cell center temperature was used to verify the accuracy of the first cell center temperature from the Navier-Stokes calculations with mesh 3. Since the Navier-Stokes computations predicted closely the measured $C_f$ values at $n$ = 20,000 and at $S$ = 3.2, 5.5, 7.7, and 9.9 stations (fig. 4a), the computed static temperatures at the first cell centers at those 4 $S$ stations and at $Z$ = 0.044 were investigated

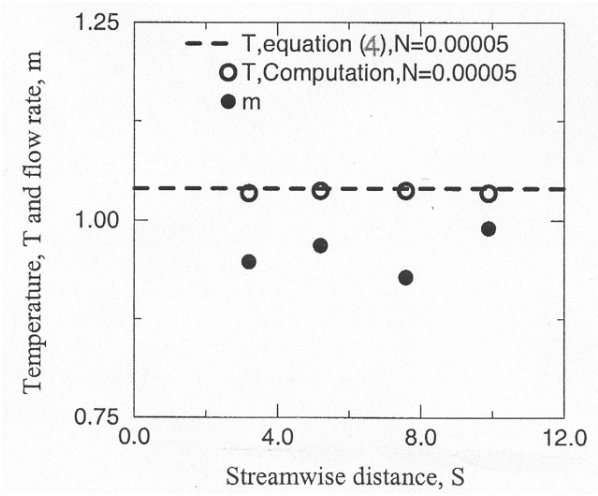


Figure 7.—Near wall temperature and flow rate at $Z$ = 0.044, $n$ = 20,000 with mesh 3.

according to equation (4) and the $Q_w$ value. The static temperatures at those cell centers obtained from the Navier-Stokes computations at $n$ = 20,000 and from equation (4) were compared in figure 7. The first cell center temperatures, from those two different approaches, were about the same at the four $S$ stations. The temperature within the flow field also depended on the mass flow rate conservation at stream-wise stations. The mass flow rates,

$$m = \int_0^{0.5} \rho V_s \partial N \qquad (5)$$

within the $S$ and $N$ plane at $S$ = 3.2, 5.5, 7.7, and 9.9 stations and at $Z$ = 0.044 were computed and their values were also plotted in figure 7. The mass flow rate was well preserved at these $S$ stations. The computations used the Reynolds analogy to model the turbulence contribution to the energy equation. Experiments (ref. 7) showed that the turbulent Prandtl number varied along the $N$ direction at $S$ = 5.3 and 9.9 stations. Based on the Prandtl number profiles, an averaged Prandtl number = 0.75 was used in the present Navier-stokes computations. The effect of different Prandtl number on the computations was not investigated here.

Experiments (ref. 7) also measured the Reynolds shear stress component, at locations along $N$ direction at $S$ = 5.3 and 9.9 stations. The present author used these measurements to verify the accuracy of the Reynolds stress simulations in the present Navier-Stokes computation. The Reynolds shear stress component at each cell center was computed using equation (3) and velocity components at each cell center location. The computed Reynolds shear stresses, $-\overline{u'v'}$ at the cell centers along direction at $n$ = 20,000, $Z$ = 0.044 and at the $S$ = 5.3 and 9.9 were plotted in figure 8a. These results were also compared, in the figure, with the measured shear stresses (ref. 7). The computed stresses were very small at $S$ = 5.3 station and did not show the rapid decrease in the

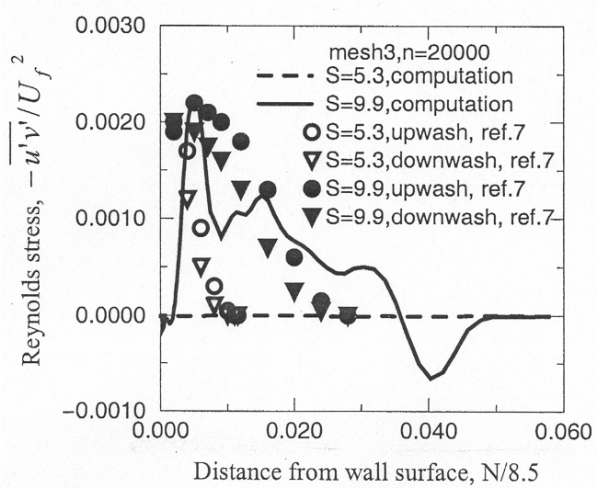


Figure 8a.—Reynolds shear stress profiles at $S$ = 5.3, 9.9, $Z$ = 0.044 and mesh 3.

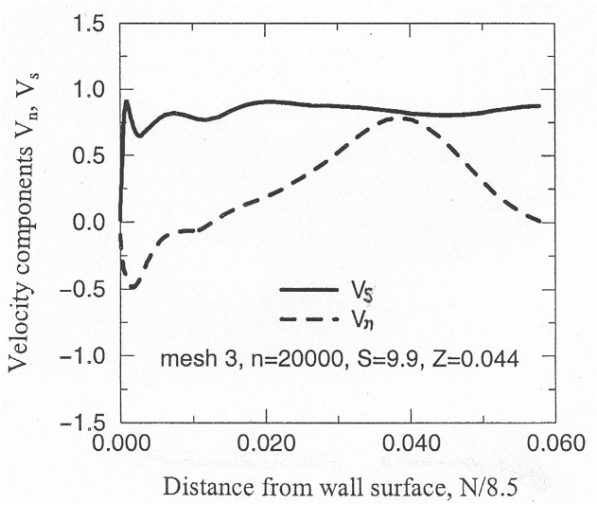


Figure 8b.—$V_s$ and $V_n$ profiles along $N$ direction, $S$ = 9.9, $Z$ = 0.044 and mesh 3.

shear stress within a small distance from the wall surface. The computed shear stresses at locations along the $N$ direction at $S$ = 9.9 agreed well with their measurements. The measurements showed the effect of the direction of the normal velocity component, $V_n$, on the shear stress values. The downwash ($V_n$ pointed toward the wall surface) reduced the shear stress value. The computed tangential and normal velocity components, $V_s$ and $V_n$ at the cell center locations along the $N$ direction at $S$ = 9.9 are plotted in figure 8b. The computations predicted downwash ($V_n$ < 0) at $N$/8.5 < 0.012 and upwash ($V_n$ > 0) at $N$/8.5 > 0.012 locations. The computed Reynolds shear stresses (fig. 8a) at the near surface locations reduced to the measured values with the downwash condition and then the computed shear stress increased, at locations away from the surface, to the measured values with upwash conditions.

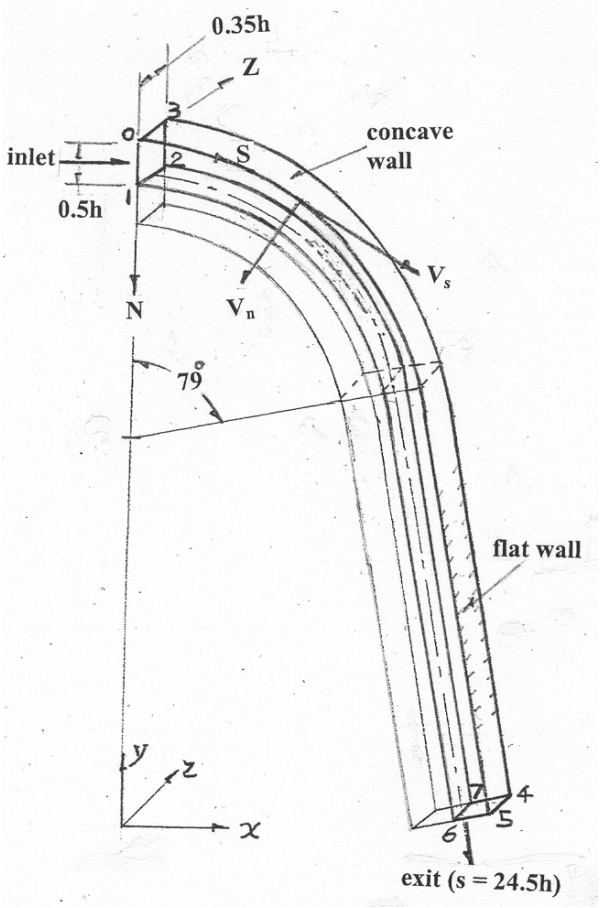


Figure 9.—Schematic of flow over concave wall with extension wall and domain 0-3-4-5-6-7-2-1.

**Flow Over Concave Wall With Extension Flat Wall**

A sketch of the flow field and corresponding physical domain for the computations was shown in figure 9. The present computations used a computational mesh configuration (mesh 5) which had node dimensions of 405 in $X$ direction, 91 in $N$ direction, and 37 in $Z$ direction. The inlet turbulence parameter, $\chi_i$, was 0.125 and the downstream static pressure, $p_d$ was 0.93 which were also used in the previous computations (ref. 6) with a different computational mesh (mesh 6). Table III listed a summary of the important parameters of the two computational meshes. A similar node spacing was assigned at the domain boundaries in both mesh configurations but large number of nodes was used in mesh 5 to reduce the node spacing along the $N$ direction.

TABLE III.—NODE CONFIGURATIONS OF MESHES 5 AND 6.

| Mesh ID | Node Size | $\Delta N$ at $N = 0$ | $\Delta N$ at $N = 0.5$ | $\Delta S$ at $S = 0$ | $\Delta S$ at $S = 24.5$ |
|---|---|---|---|---|---|
| 5 | 405,91,37 | 0.0001 | 0.030 | 0.030 | 0.090 |
| 6 | 405,61,37 | 0.0001 | 0.030 | 0.030 | 0.090 |

The present computations (with mesh 5) showed that friction factors converged at 13,000 steps of time iteration. Then, computations were investigated for the accuracy to predict the skin friction factor and mean flow velocity, and the Reynolds shear stress modeling within the flow over the upstream concave wall surface.

The computed skin friction factors, $C_f$, at all $S$ stations at $Z$ = 0.01 and $n$ = 13,000 are plotted in figure 10. $C_f$ values obtained from previous computations (ref. 6) with mesh 6 are also plotted in this figure. The computations with mesh 5 or mesh 6 calculated almost the same $C_f$. The $C_f$ value oscillated at downstream stations and the mean of $C_f$ was about 0.002. This mean value was close to the skin friction factor of a fully developed flat plate turbulent boundary layer flow. Experimental results (ref. 8) of the $C_f$ values at 6 $S$ stations are shown in figure 10 for comparisons with the computed $C_f$ values at corresponding $S$ stations. The computed $C_f$ values at near $S$ = 10 stations agreed well with $C_f$ from experiment. The mean of the computed $C_f$ at downstream stations was lower than the experimental $C_f$ values at the downstream stations.

Since the computations predicted the experimental $C_f$ values at stations near $S$ = 10, the author investigated further the computational results (with mesh 5) of the near wall surface mean velocities around the $S$ = 10 station. Computed $V_s$ values at $n$ = 13,000, $N$ = 0.003, $0 < Z < 0.35$ and $S$ = 7.7 and 9.9 are plotted in figure 11 and they are compared with the velocity measurements from the experiment (ref. 8). The experimental data was slightly shifted along the $Z$ direction for better comparisons. Comparisons showed that computations predicted well the $V_s$ variation along the $Z$ direction. Similar computational results from the previous computations (ref. 6) (with mesh 6) are shown in figure 12. The computed $V_s$ oscillated along $Z$ direction especially at the $S$ = 9.9 station. This was different from the computational results in figure 11. This showed the mesh effect on the $V_s$ computations. The computations with mesh 5 predicted more closely the experimental $V_s$ at near surface locations.

The computed $V_s$ (with mesh 5) at cell centers along the $N$ direction at $S$ = 5.5, 7.7, and 9.9 are plotted in figure 13. Existing experiments (ref. 9) measured $V_s$ at locations along the $N$ directions at $S$ = 7.7 and 9.9 stations. The measurements are plotted in figure 13 to compare with the computed $V_s$ at $S$ = 7.7 and 9.9 stations. Both the computations and experiments showed small differences in the $V_s$ values at $N/8.5 > 0.002$ locations. However, the computed $V_s$ values were larger than the $V_s$ values from the experiments. The computations also predicted a step increase within the $V_s$ profiles at $S$ = 7.7, and $S$ = 9.9 stations. The $V_s$ measurements at $S$ = 7.7 and 9.9 did not show a step increase in $V_s$ values at large $N$ locations. Figure 14 compared the $V_s$ values at $N < 0.01$ locations and $S$ = 7.7 and 9.9 stations from the computations (with mesh 5 and mesh 6) and existing experiments (ref. 9). The computations

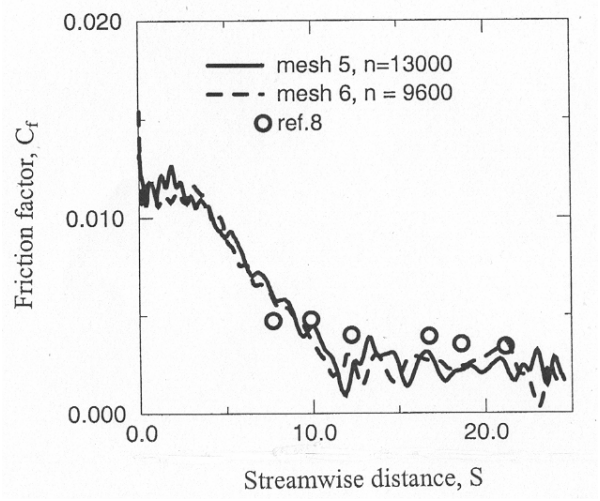


Figure 10.—Friction factors along S direction at $Z$ = 0.01 with mesh 5 and mesh 6.

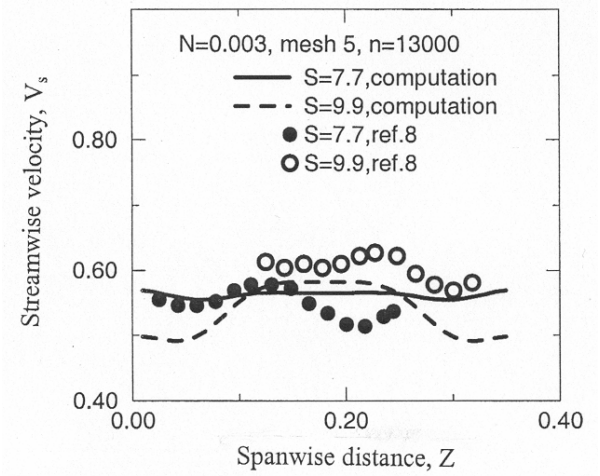


Figure 11.—Spanwise $V_s$ variations at $S$ = 7.7, 9.9, $N$ = 0.003, $n$ = 13,000, mesh 5.

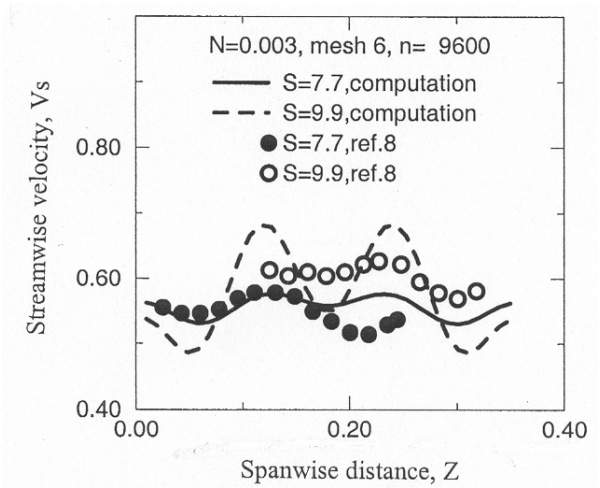


Figure 12.—Spanwise $V_s$ variations at $S$ =7.7, 9.9, $N$ = 0.003, $n$ = 9,600, and mesh 6.

predicted well the experimental $V_s$ values and the computations and mesh 5 improved the predictions of the $V_s$ at $N < 0.01$ locations. The computations also showed that $V_s$ was reduced at $S = 9.9$ station.

Equation (3) was also used to calculate the dimensionless Reynolds shear stress, $\overline{u'v'}/(dV_s)^2$, at locations along the $N$ direction at $S = 5.3$, 7.7, and 9.9 stations. The profiles of the shear stress variations along the $N$ direction at those $S$ stations are shown in figure 15. Very small shear stress was calculated at $S = 5.3$ and 7.7 stations. The shear stress appeared at the $S = 9.9$ station. The maximum stress occurred at a location where $V_s$ started to increase sharply along the $N$ direction (fig. 13). These $V_s$ and $\overline{u'v'}/(dV_s)^2$ at large $N$ locations agreed with experimental mean velocity and shear stress properties within a shear layer (ref. 14).

As flow develops along the concave wall surface, vortices might appear within the flow field. The vortices could induce upwash ($V_n > 0$) and downwash ($V_n < 0$) at the near wall surface locations (refs. 7 and 8). The downwash and upwash changed the $V_s$ profiles along the $N$ direction at near wall surface locations. The vortices could lift off from the surface and induces shear layers at large $N$ locations of downstream $S$ stations. The computational results in figure 13 were consistent with the above argument. To investigate further the occurrence of vortices, the computed velocity components $V_s$ and $V_n$ at $N = 0.00005$ (the first cell center from the wall surface), and two different $Z$ locations at $S = 5.3$ stations are plotted in terms of the time iteration step in figures 16a and b. Figure 16a was from the computation with mesh 5 and figure 16b was from the computation with mesh 6. These results showed that both $V_s$ and $V_n$ oscillated periodically at large time iteration steps ($n \approx 10{,}000$). $V_n$ also changed its direction periodically with the time step. Downwash ($V_n < 0$) increased the $V_s$ value and upwash ($V_n > 0$) decreased the $V_s$ value.

To show some effect of downstream flat plate on the flow development along a concave wall surface, the computed velocity component $V_s$ and the Reynolds shear stress $-\overline{u'v'}/U_f^2$ at $S = 9.9$ for the cases without and with the downstream flat plate are compared in figures 17a and b. Measurements (refs. 8 and 9) of $V_s$ and the Reynolds shear stress for the case without downstream flat plate are also plotted in these figures. Figure 17a showed significant difference in the values and profiles of $V_s$ at locations along $N$ direction. Different downstream static pressure boundary conditions were used respectively to perform the numerical computations for cases without and with downstream flat plate surface. The downstream pressure condition could change the $V_s$ variation. The downwash effect was significant for the case without the downstream flat plate and increased the $Vs$ value at near surface locations. The $V_s$ profile also showed possible existence of a shear layer at $0.01 < N/8.5 < 0.02$ locations and the computations calculated an increase in

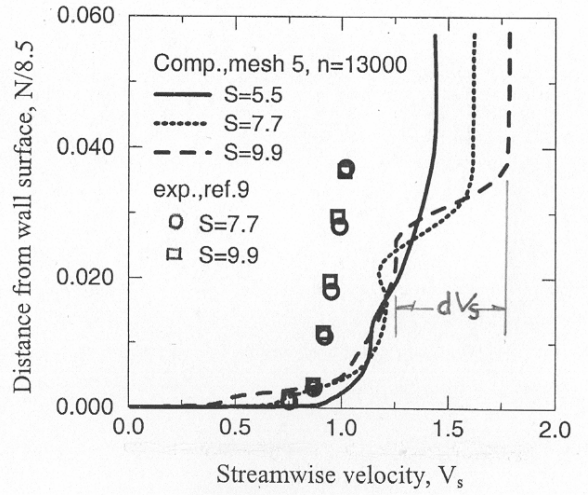


Figure 13.—$V_s$ profiles along $N$ direction at $S = 5.5$, 7.7, 9.9, $n = 13{,}000$, and mesh 5.

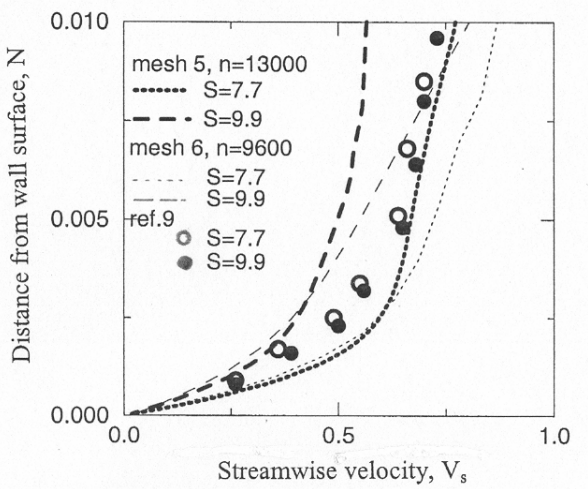


Figure 14.—Near wall $V_s$ profiles at $S = 7.7$, 9.9, $n = 13000$, mesh 5; $n = 9{,}600$, mesh 6.

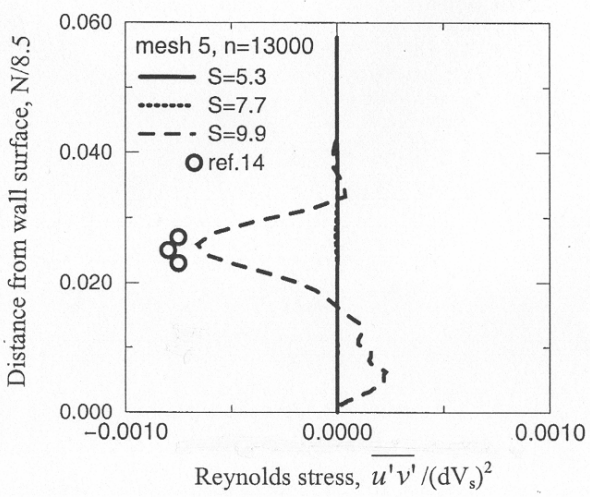


Figure 15.—Reynolds shear stress profiles along $N$ direction at $S = 5.3$, 7.7, 9.9, $n = 1$, 3000.

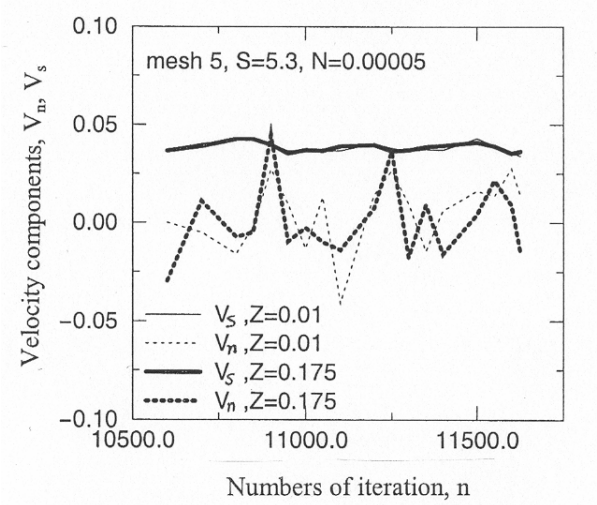


Figure 16a.—Relationship of near wall $V_s$ and $V_n$ at $Z$ = 0.01, 0.175, $S$ = 5.3, mesh 5.

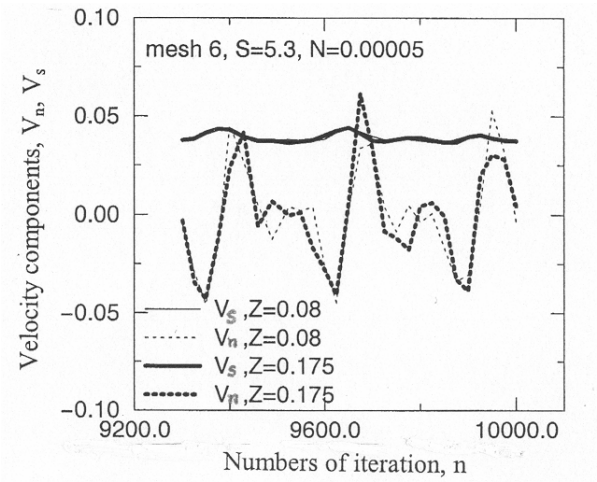


Figure 16b.—Relationship of near wall $V_s$ and $V_n$ at $Z$ = 0.08, 0.175, $S$ = 5.3, mesh 6.

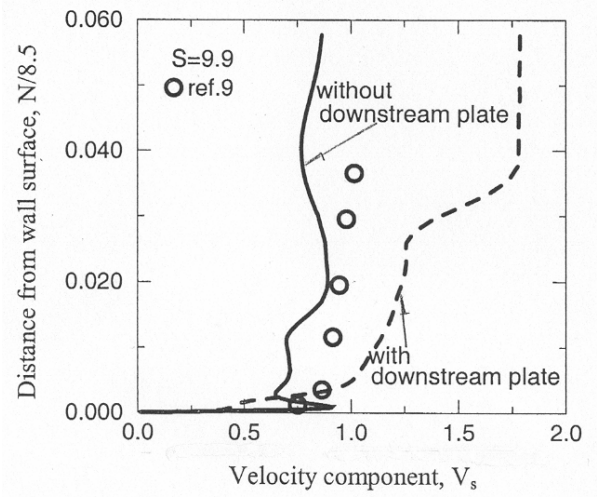


Figure 17a.—Comparisons of $V_s$ profiles without and with extension wall surface.

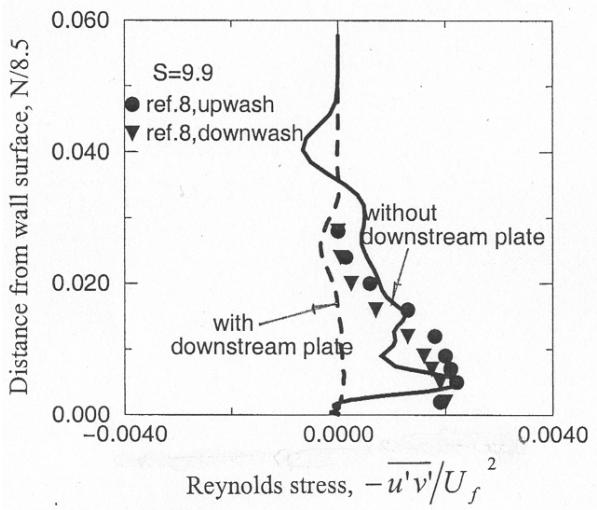


Figure 17b.—Comparisons of Reynolds shear stresses without and with extension wall surface.

the Reynolds shear stress, figure 17b, at these $N$ locations. The free shear layer occurred at $0.03 < N/8.5 < 0.04$ locations for the case with downstream flat plate. The downstream flat plate changed the flow development at locations near the concave wall surface and lifted the free shear layer further away from the wall surface. Figure 17b shows significant difference in the Reynolds shear stress predictions for the cases without and with the downstream flat plat. In turbulence modeling, the present study used different values for the empirical constant, $C_{t3}$, in the computations. $C_{t3}$ = 1.1 was used in the case without flat plate while $C_{t3}$ = 0 was used in the case with the flat plate at downstream. $C_{t3}$ = 0 was suggested (ref. 3) to model boundary layer flow development. The difference in the $C_{t3}$ value might contribute to the difference in the computed flow properties in figures 17a and b. Figure 17b also showed the computed Reynolds shear stress was small at small $N$ locations. These could be due to the turbulence modeling assumption, $\nu_t = \tilde{\nu} f_{v1}$ with $f_{v1} = \chi^3/(\chi^3 + C_{v1}{}^3)$ and $c_{v1}$ = 7.1 $\chi$ and $f_{v1}$ were small at the near surface locations which gave very small eddy viscosities at the near surface locations.

This author also made a preliminary investigation of the inlet turbulence scale effect on the computed eddy viscosities at the near wall surface locations. The author used a low Reynolds number $k$-ω turbulence model (ref. 10) to compute the turbulence eddy viscosities at the near wall surface locations within the flow over the concave wall. The computations assumed 2-D flow exited over the concave wall surface. Only Mesh 4 was used in the computations. The computations were performed respectively with two different inlet turbulence scales, $T_1$ = 0.00001 and 0.001

(non-dimensionalized with $h$) and the same inlet turbulence intensity (ref. 6), $T_u = 0.006$. The computed eddy viscosities at the near wall surface locations were compared with the eddy viscosities from the computations with One-Equation turbulence modeling. Figure 18a compared the turbulent eddy viscosities at $N = 0.00015$ and $Z = 0.044$ locations. With these two different turbulence models, the eddy viscosities had a level of $1.0 < \nu_t/\nu_{tf} < 2.0$ at all $S$ locations. The eddy viscosities were close to each other at $3.5 < S < 8.5$ stations. The $k$-ω modeling did not show significant inlet turbulence scale effect on the computed eddy viscosity. For clarity, only the results from the $k$-ω with $T_l = 0.001$ are shown in figure 18a. Figure 18b shows the computed $\nu_t$, $k$, and ω variations, due to two different inlet turbulence length scales, along $S$ direction at $N = 0.00015$ and $Z = 0.044$ location. These results did not show a strong $T_l$ effect on $\nu_t$, $k$, and ω values. These values also oscillated at $5.5 < S < 8.0$ stations. The oscillations might indicate the effect of flow transition. However, the $S$ locations were different from those from the experiment (ref. 6). This author only performed a preliminary study of $k$-ω turbulence modeling for the eddy viscosity prediction. The results indicated that the inlet turbulence scale did not have a significant effect of the eddy viscosity at the near surface locations in the flow over the concave wall surface.

Existing experiments (refs. 7 and 8) adjusted the lower wall surface geometry of curved duct flow to establish a boundary layer flow field along the concave wall surface. Measurements of the flow properties were taken within the boundary lay flow along the concave wall surface. The present study was directed toward the modeling of the flow properties at the locations near the concave wall surface, the effect of experimental lower convex wall contours on the flow development was not considered in the computations. From the experience of the present computations, the computational approach might require a huge mesh node size to model fully the experimental flow fields (refs. 7 and 8).

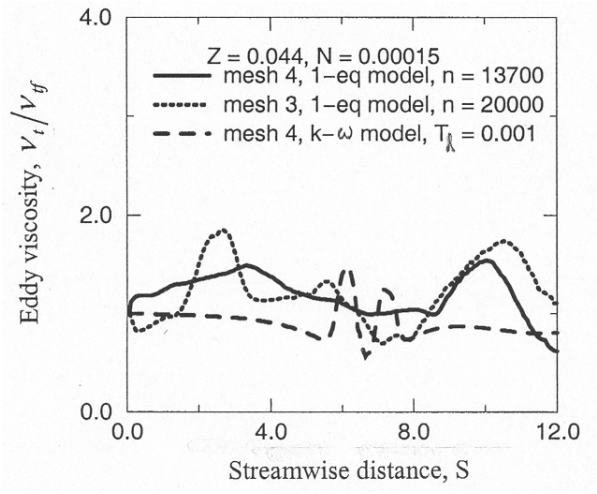


Figure 18a.—Comparisons of eddy viscosities with one-equation model and $k$-ω model.

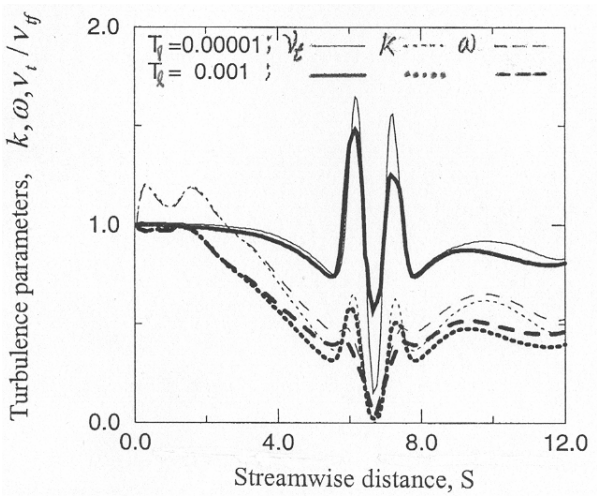


Figure 18b.—Effect of turbulence length scales on $k$-ω model, $Z = 0.044$, $N = 0.00015$ and $T_u = 0.006$.

## Conclusions

This paper presented the usage of a time marching 3-D compressible Navier-Stokes equation numerical solver and a one-equation eddy viscosity model to simulate the flow fields developed along concave wall surfaces with and without a downstream recovery flat wall. The Navier-Stokes numerical solver came from the NASA Glenn-HT RANS code. The one-equation eddy viscosity model was derived from the Spalart and Allmaras model. Although computational approach, with the Spalart and Allmaras model and RANS solver, has been used to numerically simulate complex internal and external flows. The present author believes that the approach should be studied for simple flow field simulation before being widely used for complex flow analysis. Thus, this author performed the computational simulations of boundary layer flow development along concave wall surfaces.

The author first described the governing equations and numerical schemes of the computations. The numerical computational schemes were validated for the predictions of Reynolds shear stress profile and velocity profile of a turbulent flat plate boundary layer flow. Then, the computational approach was studied for the prediction of surface friction factors, near wall surface velocity components, near wall surface temperatures and turbulent shear stresses within the boundary layer flows developed

along concave wall surfaces without and with downstream extension flat wall surface. The computational results of skin friction factor, near wall surface velocity component and temperature, and turbulent shear stress component were compared with their existing measurements and were discussed in terms of turbulence modeling, computational mesh configuration, and time iteration steps. The author concluded that:

1. With a sufficient number of node points in a structured computational mesh, the computational approach predicted the occurrence of law of the wall mean velocity profile within a flow developed along a flat wall surface. The one-equation turbulence model could provide eddy viscosities to aid the computational methods to predict accurately a Reynolds shear stress component of a fully developed flat plate turbulent boundary layer flow.
2. Given a mesh node packing condition along the normal direction to the concave wall surface, the computed skin friction factors showed the occurrence of flow transition at the upstream station. The computed skin friction factors and the near wall surface velocity components showed span-wise periodic variations as they were observed from the existing experiment. The computations predicted near wall surface temperatures which agreed well with their values derived from experimental wall heat transfer conditions. Based on the computational results of the mean velocity components and eddy viscosities, turbulence modeling of a Reynolds shear stress component agreed very well with shear stress measurements at downstream station. The computed shear stress also showed the effects of upwash and downwash on the shear stress.
3. As a preliminary step to simulate a turbine blade flow with the present computational approach, it was used to compute a developing boundary layer along a concave wall surface with a downstream extension flat wall surface. The computational approach, with a fine computational mesh, predicted the experimental measurements of the near wall velocity components better. The computed near wall surface velocity components at the upstream stations showed the vortices effects on the upwash and downwash relationship among the velocity components. The computed velocity components at locations far away from the wall surface and at downstream stations showed the occurrence of shear layer due to the vortices lift off from the wall surface at the upstream stations. Based on the computed eddy viscosity and the velocity profile, the computed Reynolds shear stress was within the range of Reynolds stress measurements from existing shear layer experiment.
4. With the aid of a low Reynolds number $k$-$\omega$ turbulence modeling, the inlet turbulence length scale was found to have little effect on the computations of the eddy viscosities at locations near the concave wall surface. The eddy viscosities from the present One-Equation turbulence modeling were comparable with the eddy viscosities from the $k$-$\omega$ modeling. Thus, the present One-equation turbulence model could be an alternate approach for turbulence modeling within flow near a solid wall surface.

The proposed computational approach could include the effect of inlet turbulence level and concave wall curvature on the simulations of developing boundary layer flows. The inlet turbulence level and wall curvature play important roles in turbine blade flow development. Thus, the present approach may have the potential to improve the turbine blade flow analysis. Since single differential equation was used to model the turbulence in the Navier-Stokes computations, the present computational approach may reduce the computational resource requirement of the Navier-Stokes simulations of complex turbine blade flows. The turbulence model approach in this work also indicated the model dependence on the Reynolds number. The present author only performed preliminary studies of the Reynolds number dependency in the work. This turbulence modeling should be further verified with existing advanced turbulence modeling

Finally, the present computational results showed the present computational approach could match the vortices effect on the near surface velocity in flow over concave wall surface. Vortices play important role in unsteady flow development. Thus, the present computational approach may lead to a foundation to develop a Navier-Stokes computational approach for the simulation of unsteady turbine blade flow field.

## References


1. Arnone, A., Liou, M.S., and Povinelli, L.A. "Multigrid Calculation of Three Dimensional Viscous Cascade Flows," AIAA 9th Applied Aerodynamics Conference, Baltimore, MD, 1991.
2. Wilcox, D.C., "Turbulence Modeling for CFD," DCW Industries, Inc., 1st edition, 1993.
3. Spalart, P.R. and Allmaras, S.R., "A one-equation Turbulence Model for Aerodynamic Flows," AIAA Paper 92–439, Reno, NV, 1992.
4. Wang, C.R., "Application of a Turbulence Model for Jet and Cross Flow Interaction," AIAA–2000–2655, Fluids 2000, Denver, CO, 2000.
5. Wang, C.R., "Preliminary Study of Vortices Effects on Flow Along a Concave Wall Surface," FD–ABS–072, 9th International Symposium on Transport Phenomena and Dynamics of Rotating Machinery, Honolulu, HI, 2002.
6. Wang, C.R., "Study of Unsteady Flows with Concave Wall Effect," AIAA–2003–4073, 21st AIAA Applied Aerodynamics Conference, Orlando, FL, June 2003.

7. Kim, J., Simon, T., and Russ, S.G., "Free-Stream Turbulence and Concave Curvature Effects on Heated, Transitional Boundary Layers," Transaction of the ASME, Journal of Heat Transfer, vol. 114, 1992.
8. Kestoras, M.D., and Simon, T.W., "Hydrodynamics and Thermal Measurements in a Turbulent Boundary Layer Recovering From Concave Curvature," Journal of Turbomachinery, vol. 114, 1992.
9. Kestoras, M.D., and Simon, T.W., "Effects of Free Stream Turbulence Intensity on a Boundary Layer Recovering from Concave Curvature Effects," ASME Paper. Presented at the International Gas Turbine and Aeroengine Congress and Exposition, Cincinnati, OH, May 1993.
10. Wilcox, D.C., "Turbulence Modeling for CFD," 1st edition, pp. 424–426, 1993.
11. Towne, C.E., Schwab, J.R., and Bui, T., "Proteus Three-Dimensional Navier-Stokes Computer Code-Version 1.0," Volume 1-Analysis Description, NASA TM-106337, 1993.
12. Kays, W.M., "Convective Heat and Mass Transfer," page 95, McGraw-Hill, 1966.
13. Klebanoff, P.S., "Characteristics of turbulence n a boundary layer with zero pressure gradient," NACA Rep. no. 1247, 1955.
14. Chang, C.T., Marek, C.J, Wey, C., and Wey, C.C., "Experimental Reacting Hydrogen Shear Layer Data at High Subsonic Mach Number," NASA Technical Paper 3342, June 1996.

# REPORT DOCUMENTATION PAGE

*Form Approved*
*OMB No. 0704-0188*



| 1. AGENCY USE ONLY (*Leave blank*) | 2. REPORT DATE | 3. REPORT TYPE AND DATES COVERED |
|---|---|---|
| | August 2005 | Technical Memorandum |

**4. TITLE AND SUBTITLE**

Navier-Stokes Computations With One-Equation Turbulence Model for Flows Along Concave Wall Surfaces

**5. FUNDING NUMBERS**

WBS–22–714–30–15

**6. AUTHOR(S)**

Chi R. Wang

**7. PERFORMING ORGANIZATION NAME(S) AND ADDRESS(ES)**

National Aeronautics and Space Administration
John H. Glenn Research Center at Lewis Field
Cleveland, Ohio 44135–3191

**8. PERFORMING ORGANIZATION REPORT NUMBER**

E–15200

**9. SPONSORING/MONITORING AGENCY NAME(S) AND ADDRESS(ES)**

National Aeronautics and Space Administration
Washington, DC 20546–0001

**10. SPONSORING/MONITORING AGENCY REPORT NUMBER**

NASA TM—2005–213830

**11. SUPPLEMENTARY NOTES**

Responsible person, Chi R. Wang, organization code RTT, 216–433–5865.

**12a. DISTRIBUTION/AVAILABILITY STATEMENT**

Unclassified - Unlimited
Subject Categories: 02 and 34

Available electronically at http://gltrs.grc.nasa.gov

This publication is available from the NASA Center for AeroSpace Information, 301–621–0390.

**12b. DISTRIBUTION CODE**

**13. ABSTRACT** ***(Maximum 200 words)***

This report presents the use of a time-marching three-dimensional compressible Navier-Stokes equation numerical solver with a one-equation turbulence model to simulate the flow fields developed along concave wall surfaces without and with a downstream extension flat wall surface. The 3-D Navier-Stokes numerical solver came from the NASA Glenn-HT code. The one-equation turbulence model was derived from the Spalart and Allmaras model. The computational approach was first calibrated with the computations of the velocity and Reynolds shear stress profiles of a steady flat plate boundary layer flow. The computational approach was then used to simulate developing boundary layer flows along concave wall surfaces without and with a downstream extension wall. The author investigated the computational results of surface friction factors, near surface velocity components, near wall temperatures, and a turbulent shear stress component in terms of turbulence modeling, computational mesh configurations, inlet turbulence level, and time iteration step. The computational results were compared with existing measurements of skin friction factors, velocity components, and shear stresses of the developing boundary layer flows. With a fine computational mesh and a one-equation model, the computational approach could predict accurately the skin friction factors, near surface velocity and temperature, and shear stress within the flows. The computed velocity components and shear stresses also showed the vortices effect on the velocity variations over a concave wall. The computed eddy viscosities at the near wall locations were also compared with the results from a two equation turbulence modeling technique. The inlet turbulence length scale was found to have little effect on the eddy viscosities at locations near the concave wall surface. The eddy viscosities, from the one-equation and two-equation modeling, were comparable at most stream-wise stations. The present one-equation turbulence model is an effective approach for turbulence modeling in the near solid wall surface region of flow over a concave wall.

| 14. SUBJECT TERMS | 15. NUMBER OF PAGES |
|---|---|
| Computational fluid dynamics; Turbulence; Turbulence model | 22 |
| | 16. PRICE CODE |

| 17. SECURITY CLASSIFICATION OF REPORT | 18. SECURITY CLASSIFICATION OF THIS PAGE | 19. SECURITY CLASSIFICATION OF ABSTRACT | 20. LIMITATION OF ABSTRACT |
|---|---|---|---|
| Unclassified | Unclassified | Unclassified | |